Liquid film dynamics during meniscus oscillation

Xiaolong Zhang, Vadim S Nikolayev

Liquid film dynamics during meniscus oscillation

Xiaolong Zhang and Vadim S. Nikolayev
Université Paris-Saclay, CEA, CNRS, SPEC, 91191 Gif-sur-Yvette Cedex, France

E-mail: xiaolong.zhang@cea.fr

Abstract. To describe the functioning of pulsating heat pipe, one needs to understand the dynamics of evaporation of thin liquid films deposited by the oscillating meniscus inside a heated capillary. Following the theory of Taylor bubbles, the dynamic profile of the liquid-vapor interface is calculated within a 2D numerical approach using the lubrication approximation. First, the steady vicinity of the contact line is analyzed under evaporation for the partial wetting case to find a relation between the microscopic and apparent contact angles. Next, the film evolution driven by the oscillating meniscus with a pinned contact line is discussed under adiabatic conditions. Finally, the evaporation of oscillating film is considered. It is shown that the film oscillation with a pinned contact line is impossible when the capillary superheating exceeds a threshold; the contact line receding needs to be taken into consideration.

1. Introduction

Pulsating Heat Pipe (PHP), a heat transfer device that is made out of a simple capillary tube, usually contains a sequence of liquid plugs and vapor bubbles of the same substance. These bubbles have a length much larger than the tube radius. In a properly functioning PHP, the liquid plugs oscillate between the evaporator (heated section) and the condenser (cooled section). Liquid films that are deposited when the menisci recede, provide the principal channel for the heat and mass exchange in PHP [1].

Previous studies have established a relationship between the film thickness and the velocity of constant receding meniscus, under the adiabatic conditions [2–4]. Additionally, the film thinning due to evaporation has been investigated in the case of the continuous liquid film on tube wall [5–7].

However, in practice, because of the evaporation, the liquid film rupture occurs in the evaporator of PHP, creating the triple contact lines where the heat and mass transfers are intense. It leads to a singularity in a narrow vicinity of the contact line, where the film thickness approaches zero and the evaporation rate in extremely high. Janeček and Nikolayev [8] present a theoretical model that relaxes this singularity by accounting for the Kelvin effect. Nonetheless, the impact of meniscus oscillation was not included.

In this article, we consider the simplest oscillation case, where the contact line is immobile (pinned on a surface defect). In order to investigate the film evolution during meniscus oscillation and with wall superheating, a 2D model that describes the dynamics of liquid-vapor interface has been developed. This work is twofold. First, we focus on the vicinity of the immobile contact line under evaporation by ignoring the meniscus motion. Next, we analyze the contact

angle response to the meniscus oscillation under adiabatic conditions. Finally, we simulate both effects together.

2. Description of the two-dimensional physical model

Consider a circular capillary tube of an inner radius R, containing a liquid plug and a long vapor bubble of the same fluid. Due to the film evaporation, a contact line appears and is pinned. The physical processes and the vapor-liquid interface are assumed to be symmetric with respect to the tube axis, and film thickness h is small as compared with the radius, $h \ll R$. Therefore, the problem can be described in 2D, in the cross-section plane of the tube, shown in Fig. 1.

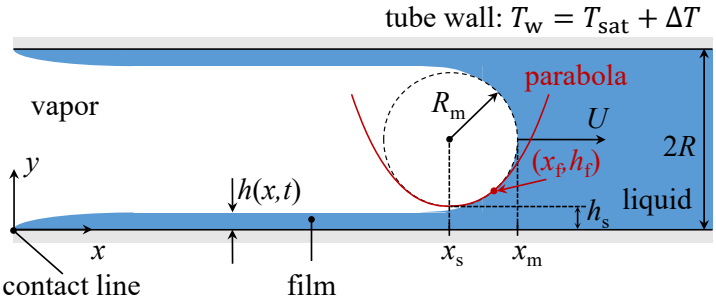

Figure 1. Meniscus moving through a capillary tube filled with liquid; the contact line is pinned at $x = 0$.

The tube is assumed to be thin enough to make the gravity force negligible. Because the vapor density and viscosity are small compared to the liquid, one can safely assume that the vapor pressure p is spatially homogeneous in the bubble and neglect the vapor-side viscous stress on the liquid-vapor interface.

Adopting the classical Bretherton approach [3], the interface is divided into the film and meniscus regions. In the film region, the interface is nearly flat ($|\partial h/\partial x| \ll 1$), it can thus be described with the lubrication approximation of the hydrodynamics equation. The meniscus region is the part of interface situating in the tube center, where the interface is controlled by the surface tension alone, thus being of constant curvature (shown in Fig. 1 with a circle of radius R_m and center at x_s).

With aforementioned assumptions, the lubrication theory [9] for the film region results in the equation that describes the interface dynamics,

$$\frac{\partial h}{\partial t} + \frac{\partial}{\partial x}\left(\frac{h^3}{3\mu}\frac{\partial \Delta p}{\partial x}\right) = -\frac{J}{\rho}, \tag{1}$$

where $h = h(x,t)$ is the local film thickness, and J is the mass flux across the interface defined to be positive at evaporation. Here, μ and ρ are the liquid shear viscosity and density, respectively. Δp is the interface pressure jump.

Conventional hypotheses concerning the liquid film mass exchange [9] are applied. A linear temperature profile in the radial direction is assumed in the thin liquid film, thus the energy balance at the interface results in the mass flux

$$J = \frac{k(T_w - T_{int})}{h\mathcal{L}}, \tag{2}$$

where T_{int} is the temperature of the vapor-liquid interface, k is the liquid heat conductivity, and $\mathcal{L}$ is the latent heat. The problem is formulated here for a general case where the tube wall can be superheated or subcooled with the respect to the saturation temperature T_{sat} corresponding to the imposed vapor pressure p. The wall superheating is denoted ΔT. The tube wall temperature

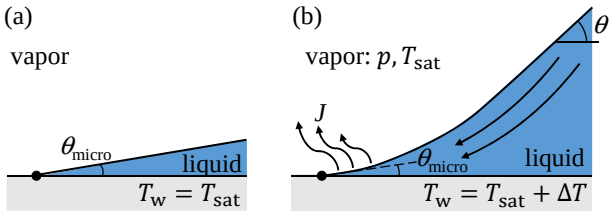

Figure 2. Sketch of the straight liquid wedge with no phase exchange (a), and curved wedge at evaporation (b).

thus is $T_w = T_{sat} + \Delta T$. The pressure jump $\Delta p = p - p_l$ (with p_l, the liquid pressure) across the interface obeys the Laplace equation

$$\Delta p = \sigma \left(K + \frac{1}{R - h} \right) \simeq \sigma \left(\frac{\partial^2 h}{\partial x^2} + \frac{1}{R_m} \right), \tag{3}$$

where σ is the surface tension, K is the 2D interface curvature in the axial cross-section shown in Fig. 1; in the small-slope approximation, $K \simeq \partial^2 h / \partial x^2$. Because of this limitation, such a film theory is not able to describe the meniscus region. The radial contribution to the curvature R_m^{-1} is assumed to be independent of x, because h is much smaller than R. At large x, Eq. (1) results in an increasingly larger h, where the surface tension gradually predominates over the viscous forces and controls the interface, so its curvature $\partial^2 h / \partial x^2$ becomes constant. Such a condition corresponds to a parabolic shape in the axial plane. This parabola matches the circular meniscus, which results in the condition

$$\partial^2 h / \partial x^2 |_{x = x_f} = R_m^{-1}, \tag{4}$$

defined at the ending point (x_f, h_f) of the film region.

2.1. Relaxing the contact line singularity with the Kelvin effect

If the vapor-liquid interface was at a fixed saturation temperature ($T_{int} = T_{sat}$), the mass flux J (Eq. 2) would diverge at the contact line $h = 0$ as $J \sim \Delta T / h$, which is nonphysical because total evaporated mass (the integral of J) would be infinite.

The Kelvin effect, i.e. the dependence of T_{int} on the interfacial pressure jump Δp

$$T_{int} = T_{sat}[1 + \Delta p / (\rho \mathcal{L})] \tag{5}$$

can relax the singularity [8], because it allows T_{int} to vary along the interface. Equations (2, 5) result in

$$J = [\Delta T - \Delta p T_{sat} / (\rho \mathcal{L})] k / (h \mathcal{L}). \tag{6}$$

T_{int} now can attain the wall temperature T_w at the contact line, which results in $J(x \to 0) = 0$ and $\Delta p(x \to 0) = \Delta p_{cl}$, where a constant pressure jump at the contact line is introduced: $\Delta p_{cl} = \mathcal{L} \rho \Delta T / T_{sat}$. By combining Eqs. (1, 6), one obtains the governing equation.

Unlike other microscopic approaches [10], the problem is now regular (i.e. Δp is not divergent). As the Kelvin effect alone is capable of relaxing the contact line singularity, the other microscopic effects such as hydrodynamic slip, Marangoni effect, and interfacial kinetic resistance [8] are not crucial. They are not included in our model for the sake of clarity.

3. Contact line model with fixed contact angle and substrate superheating

Consider now the steady case, where the meniscus motion is ignored and the contact angle is fixed.

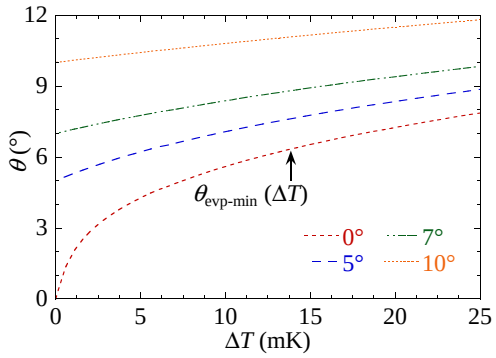

Figure 3. θ as a function of ΔT for different $\theta_{\rm micro}$ computed for pentane at 1 bar. The curve for $\theta_{\rm micro} = 0$ corresponds to $\theta_{\rm evp-min}(\Delta T)$.

When $T_{\rm w} = T_{\rm sat}$, the liquid forms a straight wedge near the contact line, as shown in Fig. 2a. When the substrate is heated, a flow inside the wedge brings the liquid towards the contact line to compensate the mass loss due to evaporation, thus creates a viscous pressure drop. Interfacial curvature forms near the contact line [1], which creates a difference between the microscopic contact angle $\theta_{\rm micro}$, the actual slope at the contact line, and the interface slope θ farther away from the contact line, cf. Fig. 2b. The characteristic length for this effect is $\ell_{\rm K} \sim 10 - 100$ nm [11] from the contact line. At the length scale $x_{\rm meso} \gg \ell_{\rm K}$ but much smaller than the film thickness $\sim 10\,\mu$m, one can define the experimentally measurable interface slope θ called the apparent contact angle. Their relationship, cf. Fig. 6a, can be expressed as

$$\theta = \theta(\Delta T, \theta_{\rm micro}), \tag{7}$$

The region $x < 0 < x_{\rm meso}$ is often referred to as microregion. Numerical calculation of θ has been completed by Janeček and Nikolayev [8]. It is based on the steady version of Eq. (12) (i.e. with $\partial h/\partial t = 0$) solved with the boundary conditions (8a). Instead of using $\Delta p_{\rm cl} = \mathcal{L}\rho\Delta T/T_{\rm sat}$, the weaker form (the second equation of (8a)) was employed for numerical proposes.

Other two boundary conditions for this fourth order differential equation are the imposed slope $\theta_{\rm micro}$ at the contact line and the condition of zero (microregion scale) curvature (8b):

$$h\,(x = 0) = 0, \qquad \partial\Delta p/\partial x|_{x\to 0} = 0, \tag{8a}$$

$$\partial h/\partial x|_{x=0} = \theta_{\rm micro}, \qquad \partial^2 h/\partial x^2|_{x=x_{\rm meso}} = 0. \tag{8b}$$

Note that the interface slope saturates at $x \gg \ell_{\rm K}$, θ is thus independent of $x_{\rm meso}$.

Figure 3 demonstrates an example of θ as a function of $\theta_{\rm micro}$ and ΔT for pentane at 1 bar, cf, Eq. (7). $\theta(\Delta T, \theta_{\rm micro})$ monotonously grows with both $\theta_{\rm micro}$ and the evaporation intensity controlled by ΔT; evidently, $\theta(\Delta T = 0) = \theta_{\rm micro}$.

One now introduces

$$\theta_{\rm evp-min}(\Delta T) \equiv \theta(\Delta T, \theta_{\rm micro} = 0), \tag{9}$$

which is a lower bound for $\theta(\Delta T, \theta_{\rm micro})$, i.e. its value for the complete wetting case [11]. Therefore, $\theta_{\rm micro} = 0$ curve in Fig. 3 represents $\theta_{\rm evp-min}(\Delta T)$. For example, for ΔT =25 mK, one obtains $\theta_{\rm evp-min}(\Delta T = 25\,{\rm mK}) \simeq 7.8°$, which signifies that the apparent angle θ will always be larger than 7.8° at this ΔT value, whatever are the wetting conditions.

4. Interface profile and contact angle during meniscus oscillation

In this section, an adiabatic problem is considered, $\Delta T = 0$ and $\Delta p_{\rm cl} = 0$, which means $\theta = \theta_{\rm micro}$. The mass exchange appearing at the macroscopic scale is insignificant and can be safely

neglected. A meniscus oscillates from the pinned contact line. The center of meniscus x_m, which is the experimentally measurable quantity, travels periodically with a period P and an amplitude A. One can assume its harmonic oscillation

$$x_\mathrm{m}(t) = x_\mathrm{i} + A[1 - \cos(2\pi t/P)], \tag{10}$$

where x_i is the initial meniscus center position. Initially, the equilibrium profile satisfying this condition $\partial h/\partial t = 0$ is used in Eq. (1). The contact line is pinned at $x = 0$. The contact angle θ_micro is expected to vary between the static advancing θ_adv and the static receding θ_rec angles (the difference of which defines the wetting hysteresis) while the contact line remains immobile.

The governing equation is solved for $x \in [0, x_\mathrm{f}]$. The boundary conditions are Eqs. (4, 8a) and the condition $h(x = x_\mathrm{f}) = h_\mathrm{f}$ where h_f is yet to be defined. As explained in sec. 2, the condition (4) means that the solution matches a parabola at $x = x_\mathrm{f}$. The parabola is in fact a small-angle approximation of the circular meniscus shape, so its geometrical parameters can be defined from those of the meniscus (cf. Fig. 1), in particular from its curvature radius and the position of circle's lowest point (x_s, h_s). The conditions of matching are both the continuity and the smoothness:

$$h_\mathrm{f} = (x_\mathrm{f} - x_\mathrm{s})^2/(2R_\mathrm{m}) + h_\mathrm{s}, \qquad \partial h/\partial x|_{x=x_\mathrm{f}} = (x_\mathrm{f} - x_\mathrm{s})/R_\mathrm{m}, \tag{11}$$

where h_s is defined with the condition $R_\mathrm{m} + h_\mathrm{s} = R$ [4]; x_s satisfies the equation $R_\mathrm{m} + x_\mathrm{s} = x_\mathrm{m}$ (cf. Fig. 1).

In the present algorithm, x_f is chosen in such a way that the difference $x_\mathrm{m} - x_\mathrm{f}$ remains constant during oscillations. This way, $h_\mathrm{f} = h(x_\mathrm{f})$ remains large with respect to the film thickness and more or less constant. As discussed in [4], the solution is nearly independent of the specific choice of h_f (and thus of x_f). The film shape and the unknown parameters (R_m, x_s, h_s, h_f) can be determined at each time moment. If the oscillation is sufficiently slow, the meniscus radius R_m is close to R throughout the oscillation but deviates from it for larger meniscus velocities.

4.1. Numerical implementation

For the harmonic oscillation case, the meniscus velocity is $U(t) = U_0 \sin(2\pi t/P)$. The velocity amplitude $U_0 = 2\pi A/P$ is convenient to be chosen as a characteristic velocity to define the capillary number $Ca_0 = \mu U_0/\sigma$. Other variables are converted into dimensionless form as (dimensionless quantities are denoted with a tilde): $x = \alpha R Ca_0^{1/3}\tilde{x}$, $h = \alpha R Ca_0^{2/3}\tilde{h}$, $t = \alpha R Ca_0^{1/3} U_0^{-1}\tilde{t}$, $p = \sigma\alpha^{-1}R^{-1}\tilde{p}$ and $T = T_\mathrm{sat}\tilde{T}$, where $\alpha \simeq 1.34$. $\alpha R Ca_0^{2/3}$ is the Bretherton film thickness [3] corresponding to the maximal receding velocity U_0.

With such a "natural" scaling four main dimensionless parameters are left: θ_i, $\tilde{P}$, Ca_0, and N. All the quantities will be studied in this parametric space. The dimensionless amplitude is linked to the period as $\tilde{A} = \tilde{P}/(2\pi)$. The governing equation in dimensionless form reads

$$\frac{\partial \tilde{h}}{\partial \tilde{t}} + \frac{\partial}{\partial \tilde{x}}\left(\frac{\tilde{h}^3}{3}\frac{\partial \Delta\tilde{p}}{\partial \tilde{x}}\right) = N\frac{\Delta\tilde{p} - \tilde{p}_\mathrm{cl}}{\tilde{h}} \tag{12}$$

where,

$$N = \mu k T_\mathrm{sat}(\mathcal{L}\rho\alpha R\, Ca_0)^{-2}, \tag{13}$$

which describes the magnitude of the Kelvin effect in the microregion.

Equation (12) is discretized using the finite volume method (FVM), which is more stable numerically [12] than the more conventional finite difference method. The variables such as h and their even order derivatives are defined at center of each grid segment (called node), while the odd order derivatives are defined at the segment ends. The FVM has the advantage that the

liquid flux is continuous at the segment ends. Nonlinear terms are managed by iteration: they include values from the previous iteration. The numerical algorithm is similar to that used by Nikolayev [9]. The mesh size is exponentially refined near the contact line (as $\tilde{x} \to 0$) to capture the contact angle variation without considerably increasing the total number of nodes [9].

4.2. Interface profile during oscillation

Fig. 4 illustrates numerical results of the interface profiles at several time moments during oscillation. The meniscus motion follows the harmonic law (10). The liquid film is deposited until $t = P/2$. For $t > P/2$, the meniscus advances over the deposited film. The interface has the wavy appearance near the end of film, resembling the ripples that appears during the steady meniscus advancing discussed in Nikolayev and Sundararaj [5]. The interface profiles $\tilde{h}(\tilde{x}, 0)$ and $\tilde{h}(\tilde{x}, \tilde{P})$ are indistinguishable, which confirms the periodicity of oscillation.

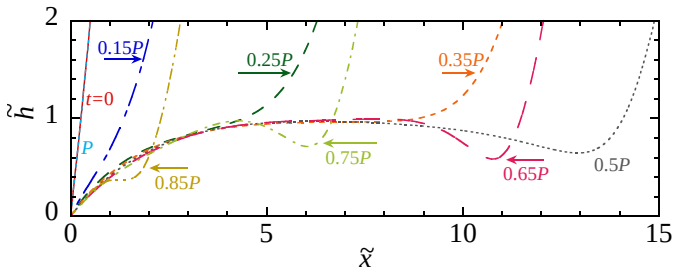

Figure 4. Periodic interface shape variation at oscillation for $\tilde{P} = 50$, $Ca_0 = 1 \times 10^{-3}$ and $\theta_\mathrm{i} = 20°$. The labels give the times corresponding to each profile, and the arrows indicate the meniscus motion direction.

The numerical results are compared with the experiments of Lips *et al.* [13]. In the experiments, a capillary tube (inner radius 1.2mm) contains two vapor bubbles and a short liquid plug of pentane. The variation of pressure difference between the vapor bubbles forces the plug oscillate, with the frequency 3.7 Hz and the velocity amplitude $U_0 = 0.24$ m/s approximately. The plug motion is recorded by the high-resolution camera and the velocity and the curvature of meniscus are then recovered from the image analysis. Because the motion is not perfectly harmonic, these experimental data were used in the numerical calculations in Eqs. (10) and (4).

In their experiments, the Weber number $We_0 = 2R\rho U_0^2/\sigma = 5.66$ is larger than unity. The Reynolds number $Re_0 = 2R\rho U_0/\mu = 1521$ is quite high and the impact of inertia on the shape of the central meniscus part must be taken into consideration. However, the thin film can still be considered as controlled by the viscosity only, because $Ca_0 \sim 3.74 \times 10^{-3}$ remains low. Under these conditions, the film ripples in the transition region close to the meniscus, which appear during the plug advancing, can be compared to the calculations.

Figure 5 presents several snapshots of plug oscillation. The left column shows the original images of Lips *et al.* [13] and the corresponding simulation results. The liquid film in transition region (in the block) is enlarged in the right column. The wavy appearance of the interface is truthfully captured by the numerical calculation.

Unfortunately, the quantitative comparison of the film thickness (i.e. the vertical coordinate) is hardly possible since the cylindrical aberration of the glass capillary is not corrected and the contact line cannot be distinguished. One can nonetheless compare the axial lengths. The size of one pixel in mm can be obtained from the known outer tube diameter (4 mm) that is visible in the original images. From the experimental images, the axial distance between the crest and the trough (Fig. 5) of the film ripple is 0.50 ± 0.02 mm, while in the simulation, it is 0.51 ± 0.01 mm. This distance is almost constant in time. Evidently, the agreement is excellent.

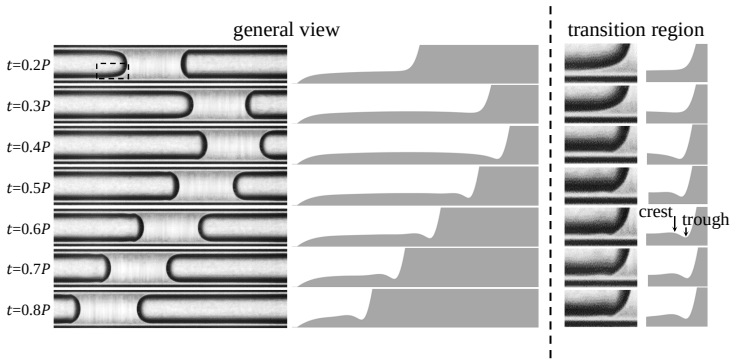

Figure 5. Liquid film shape during meniscus oscillation: comparison with experimental results by Lips *et al.* [13].

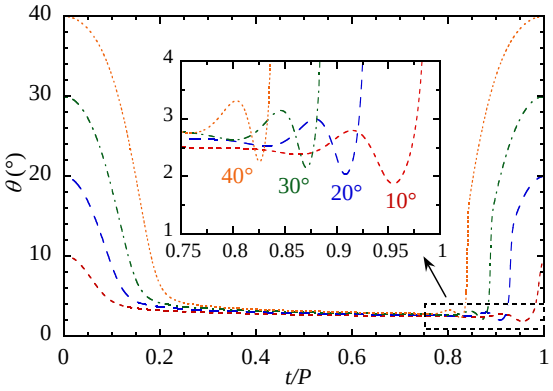

(a) Variation of contact angle during an oscillation for different values of θ_i. The inset shows enlarged undulating portions of the curves.

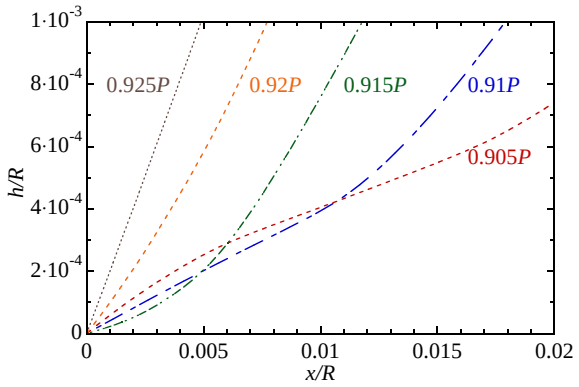

(b) The interface shape variation near the contact line around $t = 0.913P$ where θ_min is attained for $\theta_\mathrm{i} = 20°$ (cf. the inset to Fig. 6a).

Figure 6. Contact angle and interface variation for $Ca_0 = 10^{-3}$, $\tilde{P} = 50$.

4.3. Contact angle variation

A typical variation of θ during oscillation is plotted in Fig. 6a. The initial contact angle θ_i is the maximum contact angle achieved during the periodical motion.

In the beginning of a period, the capillary forces lead to the fast contact angle reduction until the meniscus recedes far enough so the curvature gradient reduces and the contact angle becomes nearly constant for a large part of a period. This nearly constant value is quite insensitive to both θ_i and P. θ slowly decreases until the ripples in the near-meniscus region approach the contact line during the backward stroke (Fig. 6b) at the end of a period. This causes the contact angle oscillations, during which its minimal value θ_min is attained:

$$\theta(t) \geq \theta_\mathrm{min}, \tag{14}$$

which depends quite weakly on θ_i (Fig. 6a). This minimal value of contact angle is of importance (cf. sec. 5 below). Since the motion is periodical, the contact angle θ_i is attained at $t = P$.

5. Combining film evaporation and meniscus oscillation

In this section we consider the meniscus oscillations together with the evaporation effect (i.e., for a positive ΔT). Two approaches are considered. First, by applying a multi-scale reasoning, we combine the results of sections 3 and 4. Second, the problem of meniscus oscillation with evaporation is solved numerically.

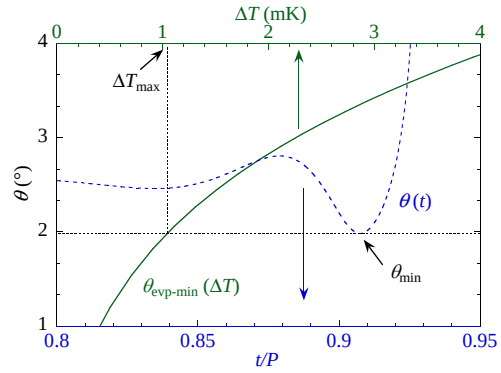

Figure 7. Function $\theta(\Delta T, 0)$ (the green line, for pentane at 1bar) plotted together with θ variation during meniscus oscillation (blue dashed line, $\theta_{\rm i} = 20°$).

5.1. Multi-scale approach

In this section we combine the above results for the case of heating conditions. Consider a case of small ΔT. The evaporation in the film and meniscus regions can thus be neglected during an oscillation period and the macroscopic results of sec. 4 still apply. However, because of the contact line singularity, the evaporation is not negligible in the microregion and leads to a difference between the apparent contact angle θ and the microscopic contact angle $\theta_{\rm micro}$, as defined in sec. 3. First, instead of solving Eq. (12) for this case, we apply here the multi-scale reasoning introduced in sec. 3.

When a solution of the full problem exists, the micro and macro regions can be matched for a given ΔT. They are connected through the relationship (7), which means the oscillatory film shape eventually imposes the value of $\theta_{\rm micro}$.

In the sprite of the multi-scale reasoning, θ must simultaneously satisfy the conditions:

1. Similarly to the case where $\Delta T = 0$, during oscillations with a pinned contact line, the moving film imposes the θ value. This implies that the inequality (14) should hold for $\Delta T > 0$, cf. Fig. 6a.

2. On the other hand, θ is defined by Eq. (7), which is bounded from below: $\theta \geq \theta_{\rm evp-min}(\Delta T)$.

The condition (ii) suggests that $\theta(t)$, throughout oscillation, should remain larger than $\theta_{\rm evp-min}(\Delta T)$. From the inequality (14), one obtains

$$\theta_{\rm min} \geq \theta_{\rm evp-min}(\Delta T), \tag{15}$$

which presents a necessary condition for matching of two regions. With the equality sign $\theta_{\rm min} = \theta_{\rm evp-min}(\Delta T_{\rm max})$, this equation defines a superheating limit $\Delta T_{\rm max}$. Since $\theta_{\rm evp-min}(\Delta T)$ is an increasing function (cf. Fig. 3), the superheating limit $\Delta T_{\rm max}$ is an upper bound. Thus the inequality (15) is satisfied when $\Delta T < \Delta T_{\rm max}$.

To determine $\Delta T_{\rm max}$ graphically, Fig. 7 presents an example where $\theta(t)$ (bottom and vertical axes, extracted from Fig. 6a) is plotted together with $\theta_{\rm evp-min}(\Delta T)$ (top and vertical axes, extracted from Fig. 3). During the oscillation, the minimum value $\theta_{\rm min} \simeq 2°$ is attained. From the dependence $\theta_{\rm evp-min}(\Delta T)$, one can deduce that $\Delta T_{\rm max} \simeq 1$ mK. A solution of oscillation problem with evaporation should be nonexistent if $\Delta T > 1$mK.

5.2. Numerical approach

In this section, we describe the results of the numerical solution of Eq. (12). In Fig. 8, variations of $\theta_{\rm micro}$ during meniscus oscillation are plotted for small ΔT of 0.2mK, 0.5mK, 0.7mK and

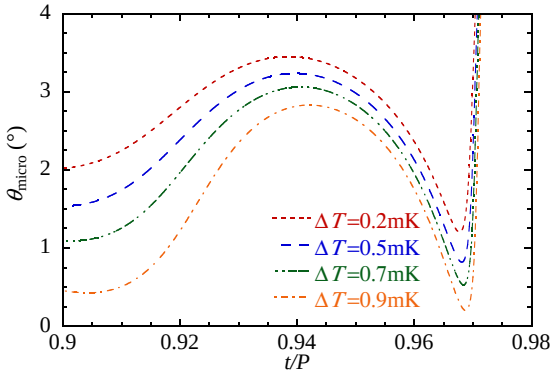

Figure 8. Variations of θ_{micro} from $t = 0.9P$ to $0.98P$, for ΔT of 0.2mK, 0.5mK, 0.7mK and 0.9mK. $\theta_{\text{i}} = 10°$, $\tilde{P} = 50$.

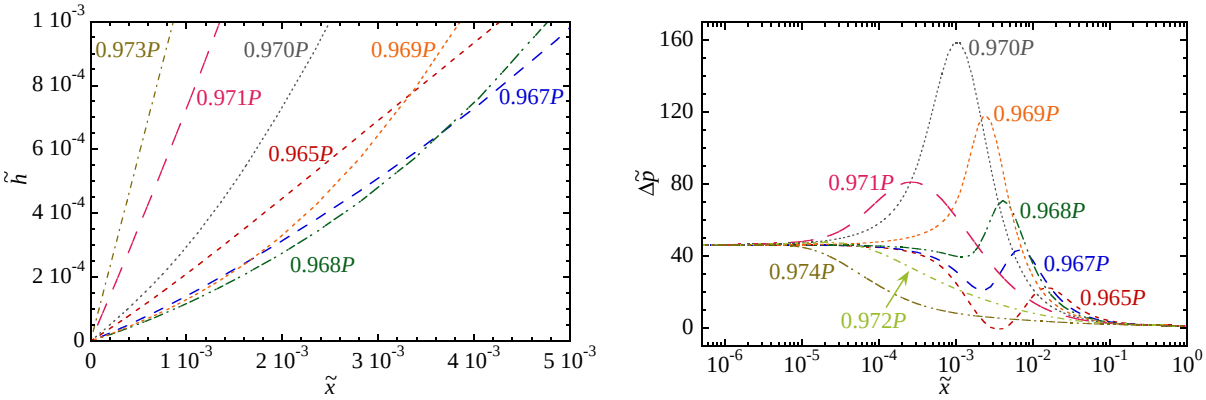

(a) Film thickness

(b) Pressure jump across the interface

Figure 9. Film thickness and pressure profiles in the micro-region around the moment $t = 0.968P$ when the minimal θ_{micro} is achieved: ΔT=0.7mK, $\theta_{\text{i}} = 10°$, $\tilde{P} = 50$.

0.9mK. θ_{micro} attains the minimal value near the time moment $t = 0.968P$. The minimum value of θ_{micro} decreases with superheating, which implies that θ_{micro} reaches zero for certain ΔT. The minimal values for ΔT = 0.2mK, 0.5mK, 0.7mK and 0.9mK, are 1.2°, 0.82°, 0.53° and 0.2° respectively. The simulations confirm that the reasoning of the previous section is correct, because the minimal value of θ_{micro} tends to zero when ΔT approaches $\simeq$ 1mK.

Moreover, the variation of θ_{micro} is strong near the minimum. It corresponds to the short time lapse when the largest ripple formed near the meniscus (cf. Fig. 4) approaches the contact line, cf. Fig. 9a. The interface curvature exhibits the rapid and strong changes near this time moment, cf. Fig. 9b. After the ripple disappearance (for $t > 0.968P$), the pressure jump quickly relaxes to the steady-state profile, in which Δp saturates towards both the contact line and the meniscus, and decreases monotonically in between, for example see the curve for $t = 0.974P$.

5.3. Paradox and its solution

Both above approaches show that the solution of the oscillation problem is nonexistent when the capillary superheating exceeds a tiny value, much smaller than the realistic superheating. The reason for this paradox is the pinned contact line: if the contact line receded, another degree of liberty would appear so the contact angle would not be constrained any more. The contact line is necessarily depinned when θ attains $\theta\,(\Delta T, 0)$ (actually, a larger value $\theta\,(\Delta T, \theta_{\text{rec}})$ but $\theta\,(\Delta T, 0)$ gives a lower bound).

As this maximum superheating is considerably smaller than that encountered in practice

(where it is rather of several degrees K, see e.g. Fourgeaud *et al.* [7]), one can deduce that the contact line receding at evaporation is inevitable and necessary to be accounted for in PHP modeling.

While the calculation has been completed here only for the pentane case, one can safely state that $\Delta T_{\max}$ is substantially smaller than realistic superheating used in thermal engineering applications for many other fluids.

6. Conclusions

Contact line effects have been investigated during meniscus oscillation and film evaporation for the simplest case, where the contact line is pinned. Apparent contact angle varies during oscillation and encounters a minimal value of several degrees. This minimal value exhibits a weak dependence on the initial value of contact angle. Because the apparent contact angle monotonically grows with the superheating for a fixed microscopic contact angle, the minimum places an upper bound for the tube superheating. This upper bound of the order of 1mK is considerably smaller than a typical experimental superheating, which means that the contact line receding is inevitable at oscillations so the dry spots should grow during the meniscus receding in the PHP evaporator. This also means the necessity to include the contact line receding when modeling the oscillation and film evaporation effects simultaneously.

Acknowledgments

The present work is supported by the project TOPDESS, financed through the Microgravity Application Program by the European Space Agency. This article is also a part of the PhD thesis of X. Z. co-financed by the CNES and the CEA NUMERICS program, which has received funding from the European Union's Horizon 2020 research and innovation program under the Marie Sklodowska-Curie grant agreement No. 800945. An additional financial support of CNES awarded through GdR MFA is acknowledged. We are indebted to S. Lips for providing us access to his experimental results.

References

[1] Nikolayev VS 2021 *Appl. Therm. Eng.* **195** 117111 doi:https://doi.org/10.1016/j.applthermaleng.2021.117111
[2] Landau LD and Levich BV 1942 *Acta physico-chimica USSR* **17** 42 doi:10.1016/B978-0-08-092523-3.50016-2
[3] Bretherton FP 1961 *J. Fluid Mech.* **10** 166 doi:10.1017/S0022112061000160
[4] Klaseboer E, Gupta R and Manica R 2014 *Phys. Fluids* **26** 032107 doi:10.1063/1.4868257
[5] Nikolayev VS and Sundararaj S 2014 *Heat Pipe Sci. Technol.* **5** 59 doi:10.1615/HeatPipeScieTech.v5.i1-4.30
[6] Chauris N, Ayel V, Bertin Y and Romestant C 2015 *Int. J. Heat Mass Transfer* **86** 492 doi:10.1016/j.ijheatmasstransfer.2015.03.013
[7] Fourgeaud L, Nikolayev VS, Ercolani E, Duplat J and Gully P 2017 *Appl. Therm. Eng.* **126** 1023 doi:10.1016/j.applthermaleng.2017.01.064
[8] Janeček V and Nikolayev VS 2012 *Europhys. Lett.* **100** 14003 doi:10.1209/0295-5075/100/14003
[9] Nikolayev VS 2010 *Phys. Fluids* **22** 082105 doi:10.1063/1.3483558
[10] Savva N, Rednikov A and Colinet P 2017 *J. Fluid Mech.* **824** 574 doi:10.1017/jfm.2017.330
[11] Janeček V, Andreotti B, Pražák D, Bárta T and Nikolayev VS 2013 *Phys. Rev. E* **88** 060404 doi:10.1103/PhysRevE.88.060404
[12] Patankar SV 1980 *Numerical heat transfer and fluid flow* (Washington: Hemisphere)
[13] Lips S, Bensalem A, Bertin Y, Ayel V, Romestant C and Bonjour J 2010 *Appl. Therm. Eng.* **30** 900 doi:10.1016/j.applthermaleng.2009.12.020